35th European Rotorcraft Forum 2009
DocumentID: 101190

HELICOPTER SLING LOAD PENDULUM DAMPING

H. Brenner
(Hanno.Brenner@dlr.de)

Deutsches Zentrum für Luft- und Raumfahrt e.V. (DLR)
Institute of Flight Systems
Braunschweig, Germany

Abstract.[1] Helicopters carrying sling loads suffer a decrease in handling qualities. In addition, the pilot control task is expanded by controlling the sling load. Both factors contribute to a significant increase in pilot workload, which can lead to a reduction in flight safety. In order to support sling load operations, the control of the load – damping and stabilization of the load pendulum swing – can be automatized by means of feedback of the load dynamic. The load pendulum controllers are integrated into an existing AFCS, featuring limitations in actuator rate and saturation. Based on a comprehensive simulation of the overall *helicopter-slings-load* system, an algorithm for the automatic determination of optimal feedback controllers has been developed. Selected controllers are tested for the potential of increasing the load pendulum damping and for the robustness under parameter variations.

Notations

Symbols

$\boldsymbol{A}$	$[-]$	system matrix
$\boldsymbol{a}$	$[m/s^2]$	acceleration $(\dot{u}, \dot{v}, \dot{w})^T$
$\boldsymbol{B}$	$[-]$	control matrix
c_S	$[N/m]$	sling spring constant
d_C	$[m]$	diameter of cylinder load
d_S	$[N\,s/m]$	sling damping constant
$\boldsymbol{F}$	$[N]$	force vector
GM	$[rad]$	gain margin
$\boldsymbol{I}$	$[kg\,m^2]$	inertia tensor
l	$[m]$	length
$\boldsymbol{M}$	$[Nm]$	moment vector
PM	$[rad]$	phase margin
S	$[m^2]$	surface
$\boldsymbol{TM}$	$[-]$	transformation matrix
(Φ, Θ, Ψ)	$[rad]$	EULER-angles
$\boldsymbol{\omega}$	$[rad/s]$	angular rates $(p, q, r)^T$
δa	$[\%]$	cyclic lateral control ($A_{1s}\,[^\circ]$)
δb	$[\%]$	cyclic longit. control ($B_{1s}\,[^\circ]$)
δc	$[\%]$	collectiv control ($\Theta_{MR}\,[^\circ]$)
δp	$[\%]$	pedal control ($\Theta_{TR}\,[^\circ]$)

Indices

A, a	aerodynamic
AP	attachment point
C	cylinder
cmd	command
cur	current
F	vertical fin
g	geodetic
H	helicopter
HCG	helicopter center of gravity
i	i-th sling
L	load
LCG	load center of gravity
LH	load hook
P	pendulum
R	rod with swivel joint
S	sling

Abbreviations

AFCS	automatic flight control system
OM	optical marker
PIO	pilot induced oscillations

1 Introduction

HELICOPTERS are designated to transport sling loads in many fields of application, for instance search and rescue operations, disaster relief, transport to remote locations, and other military support operations, respectively. However, the pilot workload is increased by the task of controlling the sling load, which implies the damping of load pendulum motions as well as the positioning of the helicopter

[1] Paper presented at the 35th European Rotorcraft Forum, Hamburg, Germany, Sept. 22-25, 2009

©DGLR 2009

and load. Due to the presence of the sling load, the dynamic behavior of the overall system is changed, compared to the helicopter without the load attached. Carrying external loads can lead to a reduction of stability margins, for eigenmodes governed by the pendulum sway motion, which can become unstable in case of improper pilot control feedback (PIO): In general, pilots cannot see the swinging load, but recognize its influence – lateral acceleration and roll – on the helicopter. If the pilot counteracts the induced lateral force, the pendulum oscillation can be further excited. Whereas, the proper control strategy would lead to a compensation of the lateral force by following the pendulum motion of the sling load. Hence, when attaching a sling load to a helicopter, the handling qualities can degrade leading to a reduction of flight safety.

The analysis of flight tests as well as incident and accident statistics reveal that the risk of these events rise with increasing pilot workload, particularly during sling load operations ([1], [2], [3], [4]). Recent trends in sling load control focus on either the manual pilot control, supported by a flight director [5], or the aerodynamic stabilization by means of fins and tails [6].

In the following, the modeling and simulation of the overall system, including a camera-based sensor model for sway detection, is described: This sensor is the basis for the development of pendulum damping controllers. The analysis of the flight dynamics of the coupled system is accomplished; relevant results are presented, which clarify the need for controlling the load pendulum motions in an analytical manner. In section 4, the structure of the control loop for the feedback of the sling load dynamics is discussed: Distinctive target values for a desirable dynamic behaviour of the overall system are defined. Section 5 deals with the development of the algorithm for the automatic derivation of the pendulum damping controllers. The performance of the closed-loop system is investigated in section 6 and evaluated regarding changes in parameters, which exert strongest influence on the flight dynamic of the overall system, such as sling length, load mass, and flight velocity, respectively.

2 System Modeling and Simulation

The modeling and simulation of the overall system *helicopter-slings-load* is supported by using MATLAB & SIMULINK®. The system is built up of two rigid-bodies – helicopter and load –, and a rod in which the slings are fitted (q.v. app., fig. 18). The rod is connected to the helicopter's single load hook and features a swivel joint in order to allow the load to turn without twisting the slings, which could elsewise exceed the load limits of the slings. The slings are modeled as flexible cables: Hence, the cable-forces represent the constraining forces within the two-body system. Different load aerodynamics can be considered. The rigid body dynamics of the helicopter, the load and the rod is discussed in the appendix.

Aerodynamics

The aerodynamic forces and moments of the helicopter ($\boldsymbol{F}^A_{H,b}, \boldsymbol{M}^A_{H,b}$) are nonlinear functions of the helicopter motion and the atmosphere, which include the relevant multi-dimensional effects sufficiently. For the present work, linear aerodynamics of a CH-53D cargo helicopter are implemented, leading to a quasi-nonlinear description of the helicopter dynamic in (50) and (51). The derivatives are obtained from [7]: They were derived by linearization of a generic nonlinear simulation code and cover a speed range from hover up to $140\,kts$ at a helicopter gross weight of 16 tons.

For the following investigations of the performance and robustness of the pendulum damping feedback control, a cylinder with vertical fins is considered as external load. It is well known that cylinders equipped with tail-fins suspended by slings, develop marginally stable eigenmodes [8]. The aerodynamic forces of the cylinder are subdivided into normal and tangential forces. The latter ones result from skin friction and impact pressure, and are summed up according to equations (57)-(60) (q.v. app.).

Due to differences in pressure distribution between the front and the back side of the cylinder, every unsymmetrical shaped cylinder develops aerodynamic moments. The cylinder is unstable around its pitch and yaw axis. The resultant moments are given by (62). For directional stability, a vertical fin is attached to the rear of the cylinder, whose aerodynamic forces and moments are determined in (64) and (65).

Constraining forces

The load carrying harness consists of one or more slings, whose dynamic properties are defined by specific spring and damping constants, depending on the sling material. Due to the relative motion between helicopter and load, the slings are elongated, resulting in forces (eq. 66), which in turn generate moments (eq. 71, 72) due to the offset between the sling attachment points and the respective center of gravity (fig. 18).

The sling forces and moments as well as the aerodynamic forces and moments are added to the vectorial forces and moments in the equations of motion (50) and (51).

Automatic flight control system

In order to stabilize the basic unstable helicopter, an AFCS is implemented according to [7] (fig. 2). It superposes the pilot inputs by ±10% in cyclic and col-

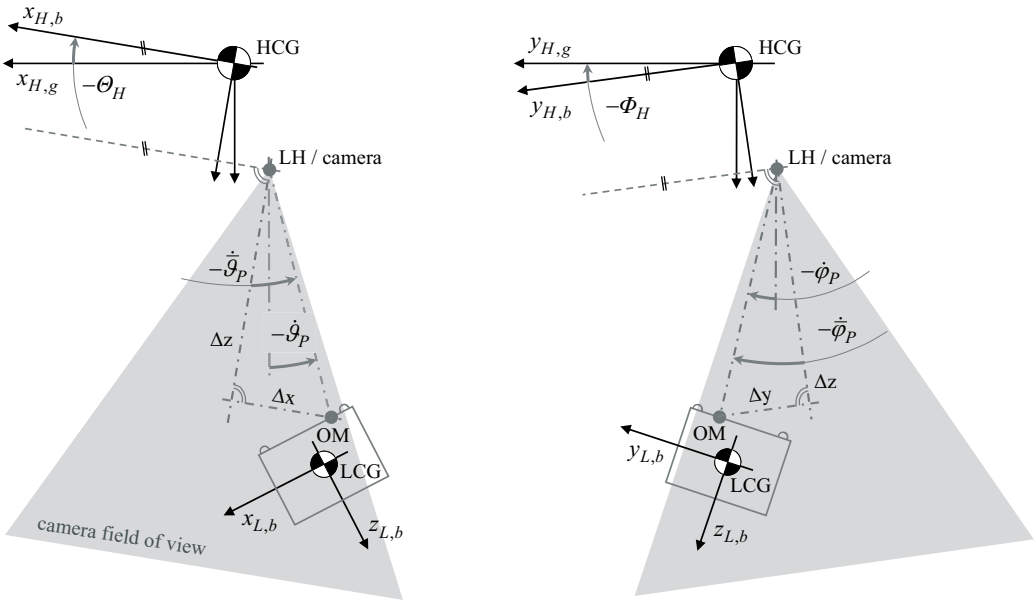

Figure 1: Sensor installation

lective control, and by ±3% in pedal control; the actuator rates are limited to $100\%/s$.

In section 4, the pendulum controllers are determined on the basis of the AFCS-controlled, and thus, stable helicopter.

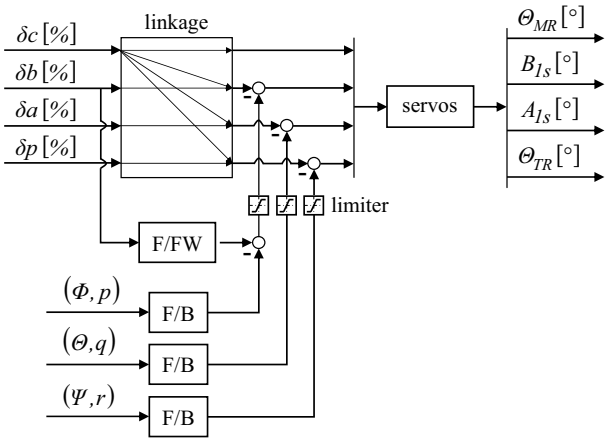

Figure 2: AFCS basic sketch

Sensor selection and modeling

The states of the model description do not deliver direct information about the load pendulum sway. Thus, the pendulum motions, which are to be controlled, must be measured and provided as output variables. Different types of sensors are considered: For instance, an IMU that is mounted on the load can measure the body rates and transmit the data to the helicopter for further processing. Another approach is the installation of a sensing arm that follows the motions of the rod as an indicator for the load dynamic.

In general, sensors that do not require to transmit the information of the load dynamic from the load system to the helicopter system are advantageous, because then system complexity is kept to a minimum, which in turn leads to higher reliability. For this reason, a camera sensor featuring digital image processing for measuring the pendulum dynamic is chosen: A camera, which is mounted underneath the helicopter, tracks an optical marker (OM), which is placed on the load or at the slings, and generates visual information of the load position and velocity with reference to the helicopter body system (fig. 1). The load pendulum angles $\dot{\bar{\varphi}}_P$ and $\dot{\bar{\vartheta}}_P$ in the helicopter body system are then determined. These data are further processed using the helicopter attitude and body rates – measured by the onboard IMU – in order to derive the controller variables $\dot{\varphi}_P$ and $\dot{\vartheta}_P$, which describe the load pendulum motion in the geodetic system.

This kind of sensor was developed by iMAR GmbH [9] and is the basis for the simulation setup. The digital image processing provides short time delays as well as sample rates, which are sufficiently high concerning the rather slow load pendulum dynamic. Figure 1 shows the mounting position of the camera; its field of view covers an opening angle of 60°, which can be extended to 180° at the expense of process time.

Besides the derivation of the system pendulum angles and rates, the digital image processing includes KÁLMÁN-filtering for the simulated prediction of the position of the optical marker. The load dynamics is

calculated by means of a simplified analytical pendulum model. This information is needed, in case the external load is not located within the camera field of view, due to large pendulum deflection angles, for instance.

State space model

The equations of motion in (50), (51) and (53) describe the overall system *helicopter and sling load*, and are used in the numerical simulation in their full nonlinear formulation. For analyses of the flight dynamics – for instance, stability and controllability – the system of equations must be simplified. For this, the state variables are bound to a working point, in order to enable a linearization: The theory of linear systems considers stationary flight conditions at an operating point $\boldsymbol{x}_0$. For the analysis and synthesis of linear systems, a multiplicity of tools – time-domain based as well as complex-variable-domain based – is available.

The linearization of the overall system leads to the state space model:

$$(1) \quad \dot{\boldsymbol{x}} = \boldsymbol{A}\boldsymbol{x} + \boldsymbol{B}\boldsymbol{u} \quad \text{(state equation)}, \ \boldsymbol{x}(0) = \boldsymbol{x}_0$$

$$(2) \quad \boldsymbol{y} = \boldsymbol{C}\boldsymbol{x} + \boldsymbol{D}\boldsymbol{u} \quad \text{(output equation)}$$

The state vector is given with

$$(3) \quad \boldsymbol{x} = [\boldsymbol{x}_H, \boldsymbol{x}_R, \boldsymbol{x}_L]^T$$

including the helicopter/load states ($\Lambda = H, L$)

$$(4) \quad \boldsymbol{x}_\Lambda = (u, v, w, p, q, r, \Phi, \Theta)_\Lambda$$

and the states of the rod

$$(5) \quad \boldsymbol{x}_R = \left(\dot{\varphi}, \dot{\vartheta}\right)_R$$

and the control vector

$$(6) \quad \boldsymbol{u} = [\delta c, \delta b, \delta a, \delta p]^T$$

as well as the output vector

$$(7) \quad \boldsymbol{y} = \left[\ (u, v, w, p, q, r, \Phi, \Theta)_H \, , \left(\varphi, \dot{\varphi}, \vartheta, \dot{\vartheta}\right)_P \ \right]^T$$

The system state matrix consists of the main matrices of the partial systems and the respective coupling matrices

$$(8) \quad \boldsymbol{A} = \begin{bmatrix} \boldsymbol{A}_H & \boldsymbol{A}_{R\to H} & \boldsymbol{A}_{L\to H} \\ \boldsymbol{A}_{H\to R} & \boldsymbol{A}_R & \boldsymbol{A}_{L\to R} \\ \boldsymbol{A}_{H\to L} & \boldsymbol{A}_{R\to L} & \boldsymbol{A}_L \end{bmatrix}$$

where the submatrix $\boldsymbol{A}_H$ contains the classical helicopter derivatives. The control matrix results in

$$(9) \quad \boldsymbol{B} = \begin{bmatrix} \boldsymbol{B}_H \\ \boldsymbol{B}_R \\ \boldsymbol{0} \end{bmatrix}$$

with $\boldsymbol{B}_L = \boldsymbol{0}$. The observer matrix is given with

$$(10) \quad \boldsymbol{C} = \begin{bmatrix} \boldsymbol{C}_H & \boldsymbol{0}_{(8x2)} & \boldsymbol{0}_{(8x8)} \\ \boldsymbol{C}_{H\to P} & \boldsymbol{C}_{R\to P} & \boldsymbol{C}_{L\to P} \end{bmatrix}$$

For the given system the feedthrough matrix is a zero matrix:

$$(11) \quad \boldsymbol{D} = \boldsymbol{0}_{(12x4)}.$$

3 Analysis of the System Flight Dynamics

The flight dynamics describes the character of the motions of the overall linear system; one important result is the stability analysis. Applied for a cubical load without aerodynamics, figures 3 and 4 show the eigenmodes of the helicopter and the load at 60 kts forward level flight. The considered weight of the cube is 3000 kg and the length of the single sling is 7 m.

The incorporated degrees of freedom within the eigenmodes were analyzed using the corresponding eigenvectors. A characterization is given in table 1. The eigenmodes *I, II, V, VI, VII, VIII* mainly describe the helicopter dynamic, slightly coupled with the load dynamic. As a coupled motion of the systems *helicopter-rod-load*, the pendulum oscillation is described by the eigenmodes *III* (lateral) and *IV* (longitudinal). A vertical oscillation of high frequency is given by *IX*: The mode couples the vertical axes of the helicopter and the load by the flexible sling. The incorporation of the dynamics of the two degrees of freedom of the rod are described in *X* and *XI*. They are both of high frequencies, because of high constraining forces acting at the rather light rod of 50 kg. Besides the pendulum motions, the single suspended cube executes pitch and roll, which finds its expression in the eigenmodes *XII* and *XIII*. Due to the lack of aerodynamic stabilization, the load's yaw motion has neutral stability, caused by the yaw hinge of the rod – it is located in the point of origin, and is not shown for clarity reasons.

Depending on system parameters like the cable length and the load mass, the eigenmodes of the overall system vary – particularly the pendulum motions in *III* and *IV*. The overall system shows a tendency to developing marginally stable pendulum motions (fig. 3 and 4). When increasing the sling length, the frequencies of the eigenmodes *III* and *IV* decrease, as well as of the vertical motion in *IX*, since the sling spring constant is a function of its length (fig. 3b).

©DGLR 2009

Table 1: Characterization of eigenmodes

eigenmode	characteristic	eigenmode	characteristic
I	helicopter roll mode	VIII	coupled helicopter longitudinal motion
II	helicopter dutch-roll mode	IX	coupled vertical oscillation
III	coupled lateral pendulum motion	X	coupled DmL lateral oscillations
IV	coupled longitudinal pendulum motion	XI	coupled DmL longit. oscillations
V	helicopter lateral- and roll mode	XII	load pitch mode
VI	helicopter roll mode	XIII	load roll mode
VII	coupled helicopter vertical motion		

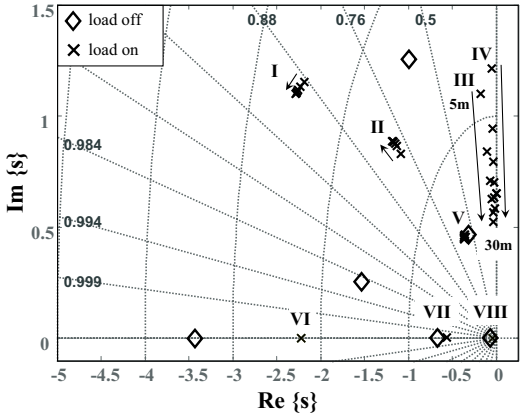

(a) close-up range

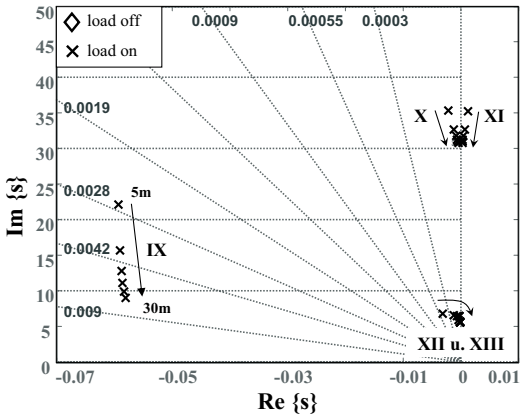

(b) far-field range

Figure 3: Pole-zero maps for a steady-state horizontal flight at $60\,kts$ with a $3000\,kg$ sling load, and a variation of sling length

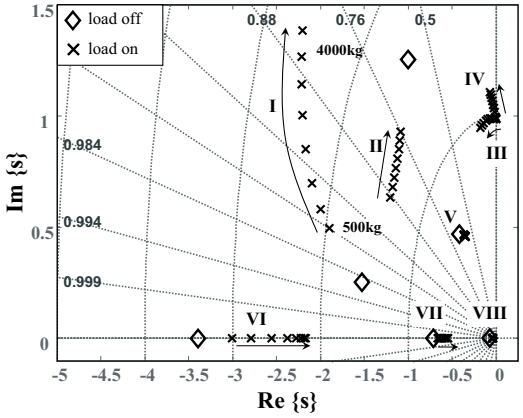

(a) close-up range

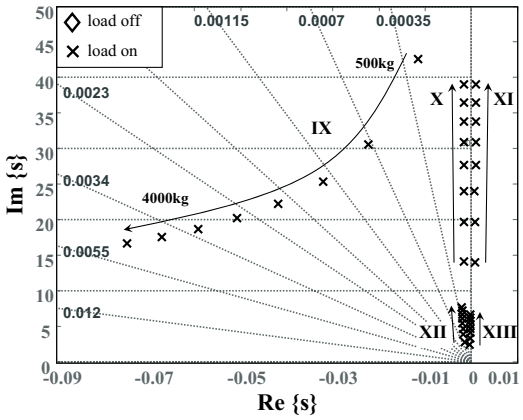

(b) far-field range

Figure 4: Pole-zero maps for a steady-state horizontal flight at $60\,kts$ with a $7\,m$ sling, and a variation of load weight

By increasing the load weight, the pendulum frequencies rise (fig. 4a). This effect can be explained by a simplified two-point dumb-bell model with the pendulum frequency given by (q.v. [10]):

$$\omega_P = \sqrt{\frac{g}{l} \cdot \left(1 + \frac{m_L}{m_H}\right)} \quad (12)$$

Since the helicopter roll rate in *I* and *II* is coupled with the load weight, the change in the pendulum frequency affects these eigenmodes, too – the damping declines with an increase in load weight. Furthermore, helicopter body-rates are controlled by the AFCS, which further amplifies the reciprocal effect of decreasing system damping as result of increasing system weight.

The stability graph of the cylinder eigenmodes is shown in figure 5. The pole *IIIa* marks the lateral pendulum swing and *IIIb* characterizes the yaw motion. For light loads and short slings, the yaw motion becomes unstable.

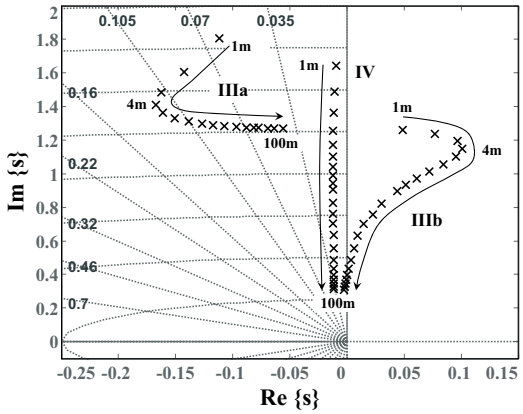

(a) sling length variation

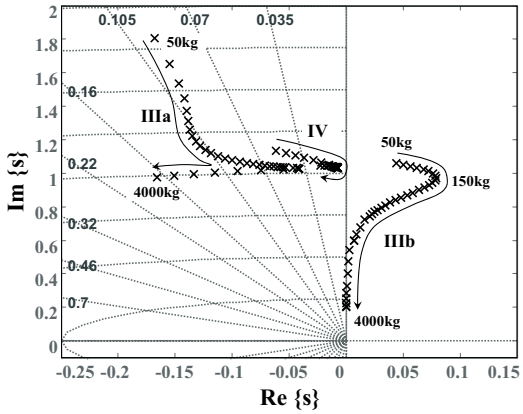

(b) load weight variation

Figure 5: Cylinder eigenmodes at $60\,kts$, $l_S = 10\,m$, $m_L = 500\,kg$

4 Pendulum Damping Controllers

In a first step, the structure of the control loop is determined. For this, the transfer functions from control inputs in $\boldsymbol{u}$ to the sensor outputs in $\dot{\varphi}_P$ and $\dot{\vartheta}_P$ are derived. By means of a DIRAC-input applying in the four different controls, both pulse responses, the lateral and longitudinal pendulum oscillations, are determined, which deliver insight into the system's main-coupling and cross-coupling. Figure 6 shows, that the lateral control δa and the longitudinal control δb lead to relevant pendulum oscillation in their relative main axis without noteworthy cross-coupling effects. The response of excited by collective control is only small. The pedal control input initially leads to a rotation and subsequently to a lateral displacement of the helicopter, which induces a lateral oscillation of the load. Hence, pedal input is not considered for pendulum damping control.

The camera sensor detects the pendulum angles and rates. Since the deflection angles of the external load may vary with different flight states, only the pendulum rates are used for feeback control. Hence, a trim-

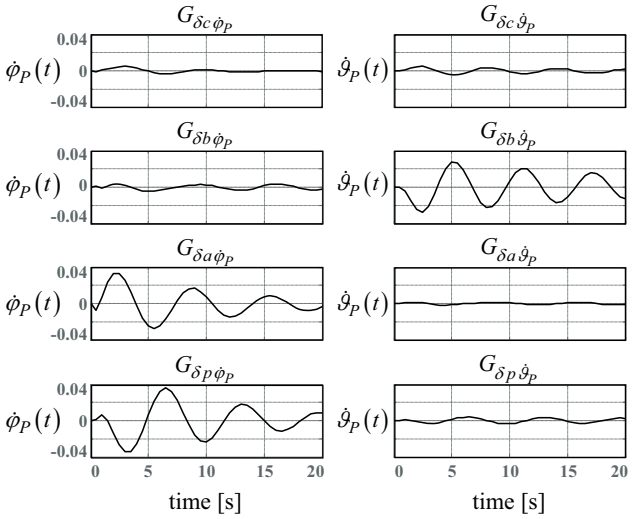

Figure 6: Impulse responses in $\left[rad\,s^{-1}\right]$ of the flight case $V = 60\,kts$, $l_S = 7\,m$, and $m_L = 3000\,kg$

-point tracing of the stationary deflection angles $\varphi_{P,cmd}$ and $\vartheta_{P,cmd}$ is not necessary, so that both angles can vary slightly without causing the controller to engage.

With the command variables $\dot{\varphi}_{P,cmd}$ and $\dot{\vartheta}_{P,cmd}$ set to zero, the control variables are given with:

$$\dot{\varphi}_P = \dot{\varphi}_{P,cmd} - \dot{\varphi}_{P,curr} \quad (13)$$

$$\dot{\vartheta}_P = \dot{\vartheta}_{P,cmd} - \dot{\vartheta}_{P,curr} \quad (14)$$

The analysis of the impulse responses leads to the assignment of the control variables to their related main

control inputs in δa and δb; any cross-coupling is disregarded. Figure 7 shows the control loop of the overall system that is expanded by the control modes for the pendulum damping. As mentioned above, the feedback inputs of the AFCS as well as the pendulum controls are limited in rate and amplitude.

In general, control loops must achieve performance requirements that refer to stability, controllability, quickness and robustness of the feedback control. For stability and damping, the system must execute pendulum motions of rapidly declining oscillation amplitudes. After experiencing a disturbance – for instance, a control input or gust –, the pendulum dynamic must return to the command input quickly and only with marginal overshooting. The time until the maximum overshoot is reached, must be minimal.

For the controller design, the requirements of the closed loop in the time-domain are translated into requirements of the open loop in the frequency-domain. In doing so, the basic demand of stability refers to a phase margin of $\Phi_{PM} > 0°$ and a gain margin of $A_{GM} < 0\,dB$. Approximating the pendulum dynamic by a $PT2$-element, the damping ζ of the closed loop is

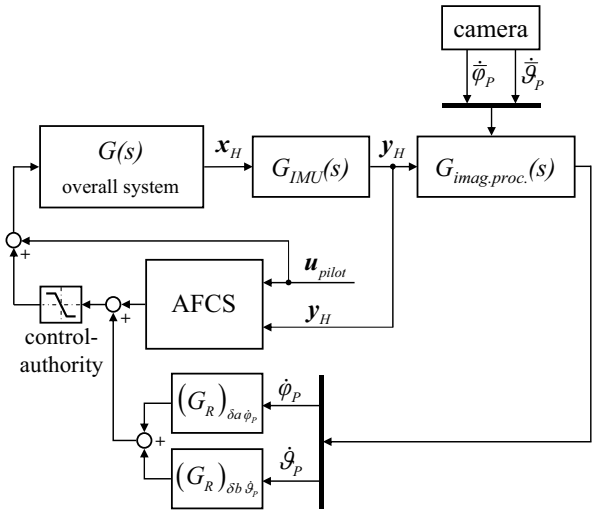

Figure 7: Feedback loop of the pendulum damping controllers

proportional to the phase margin according to:

$$(15)\quad \Phi_{PM} = \arctan \frac{2\zeta}{\sqrt{\sqrt{4\zeta^4+1}-2\zeta^2}}$$

Thus, considering the minimum damping of $\zeta > 0.2$ and the beginning of the aperiodic response at $\zeta > 0.7$, an adequate phase margin is chosen to be in the range of:

$$(16)\quad 60° \leq \Phi_{PM} \leq 90°$$

In addition to the dynamic requirements, a high static amplification of the feedback control is desirable, if it is not threatening stability. Hence, together with an appropriate behaviour in response and disturbance, the gain margin of the open loop $G_0(s)$ is chosen to be in the range of:

$$(17)\quad -3{,}5\,dB \leq (A_{GM} = G_0(j\omega_{-180°})) \leq -20\,dB$$

Furthermore, the closed loop must be fast enough in terms of meeting the system's natural pendulum frequency ω_P, at the minimum, which can be estimated using equation (12). Thus, the required gain crossover frequency is given with:

$$(18)\quad \omega_{d,cmd} = (\omega_P)_{test\,case}$$

The controller design parameters are displayed in the frequency responses of the transfer functions $G_{\delta a\,\dot{\varphi}_P}(s)$ and $G_{\delta b\,\dot{\vartheta}_P}(s)$ of the test case featuring $V = 60\,kts$, $l_S = 7\,m$, $m_L = 3000\,kg$ in figure 8.

The system eigenmodes of table 1 are illustrated. The influence of the the eigenmodes *IX* to *XIII* is marginal: They are parasitic poles. For $(\omega \to 0)$, the responses feature a distinct D-element: In case of a step input in the command variables, a control offset persists due to the missing I-element. This effect is evident since a stable pendulum oscillation is always returning to the initial states $\dot{\varphi}_P = \dot{\vartheta}_P = 0$. The decrease of the frequency responses for $(\omega \to \infty)$ marks the time-delay of the system.

A detailed analysis of the open loop frequency response over the variation of the flight speed, the sling length, and the load mass revealed that an increase in flight speed generally reduces the phase margin corresponding to a decrease in the pendulum damping. The gain margin is reduced, which degrades the robustness of the feedback control in terms of variations in static amplification. The gain cross over frequency raises slightly. Increasing the weight of the sling load leads to an increase in damping – the amplitude decreases – with only marginally shifting the cross over frequency. The shorter the slings are, the faster the pendulum motions will be, which is expressed by an increase in the cross over frequency. In this case, the phase margin and the gain margin decrease.

Particularly for a combination of high flight speeds, short slings, and light loads, the requirements that have been defined previously cannot be achieved; this means marginally stable or even unstable pendulum oscillations. Furthermore, only minor static amplifications can be accomplished in order to comply with the basic stability requirements. Thus, the frequency responses must be customized by controllers to eventually allow for high amplifications together with sufficiently high phase and gain margins. These controllers must be effective over the entire flight envelope, which is defined by the flight speed, the sling length, and the load weight, respectively.

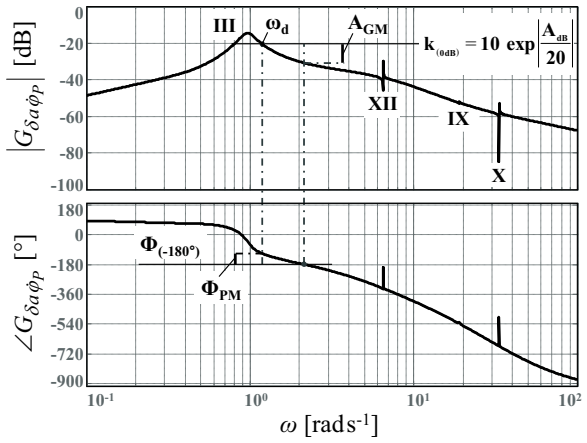

(a) $G_{\delta a\,\dot{\varphi}_P}(s)$

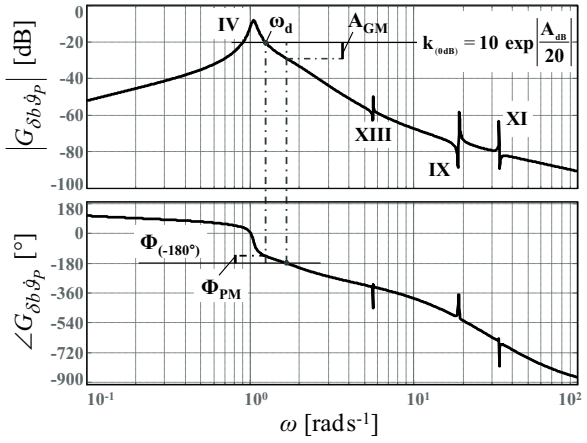

(b) $G_{\delta b\,\dot{\vartheta}_P}(s)$

Figure 8: Frequency responses of the pendulum rates of the flight case $V = 60\,kts$, $l_S = 7\,m$, $m_L = 3000\,kg$

The controllers for both pendulum directions $(G_R)_{\delta a\dot{\varphi}_P}$ and $(G_R)_{\delta b\dot{\vartheta}_P}$ each consist of two sub-controllers – $G_{PM}(s)$ for the modulation of the phase response and $G_{GM}(s)$ for the gain response:

$$G_R(s) = k_{amp} \cdot G_{PM}(s) \cdot G_{GM}(s) \tag{19}$$

The phase response controller $G_{PM}(s)$

The uncontrolled system

$$G_S(s) = \begin{cases} G_{\delta a\,\dot{\varphi}_P}(s) & \text{lateral swing} \\ G_{\delta b\,\dot{\vartheta}_P}(s) & \text{longitudinal swing} \end{cases} \tag{20}$$

is first proportional amplified by

$$k_{0dB} = 10^{\left|\frac{A(\omega_d)dB}{20}\right|} \tag{21}$$

in order to lift the gain response to the gain crossover frequency $\omega_d = \omega_P$ of the $0\,dB$-line. Hence, the quickness of the closed-loop equals the system's natural pendulum frequency. Considering the phase response of the proportional amplified open loop, the current phase margin is determined by

$$\Phi_{PM}(\omega_d) = \angle G_S(\omega_d) + 180^\circ \tag{22}$$

The actual desired phase margin $\Phi_{PM,cmd}$ is defined as a value of the intervall in equation (16). Hence, the quantiative demand on modulating the phase response is expressed by

$$\Delta\Phi_{PM}(\omega_d) = \Phi_{PM,cmd} - \Phi_{PM}(\omega_d) \tag{23}$$

The shaping of the phase response in place of the cross gain frequency ω_d is accomplished by the controller transfer function

$$G_{PM}(s) = \frac{1 + \omega_I^{-1} s}{1 + \omega_{II}^{-1} s} \tag{24}$$

which corresponds to

- a phase-lifting controller $G_{PDT1}(s)$ in case of $\omega_I < \omega_{II}$ or
- a phase-lowering controller $G_{PPT1}(s)$ in case of $\omega_I > \omega_{II}$

The respective frequency response is given with

$$G_{PM}(j\omega) = A(\omega)\, e^{j\Phi(\omega)} \tag{25}$$

with the amplitude response

$$|G_{PM}(j\omega)| = \sqrt{Re^2\{G_{PM}\} + Im^2\{G_{PM}\}}$$

$$= \sqrt{\frac{1 + \omega_I^{-2}\,\omega^2}{1 + \omega_{II}^{-2}\,\omega^2}} \tag{26}$$

and the phase response

$$\angle G_{PM}(j\omega) = \arctan\left(\frac{Im\{G_{PM}(j\omega)\}}{Re\{G_{PM}(j\omega)\}}\right)$$

$$= \arctan\left(\frac{\omega_I^{-1}\omega - \omega_{II}^{-1}\omega}{1 + \omega_I^{-1}\omega_{II}^{-1}\omega^2}\right) \tag{27}$$

The frequency $\omega_{\Phi_{max}}$ of the maximum phase-lift and phase-decline, respectively, is determined by the maximum of the phase response of the controller, which is derived by differentiation

$$\frac{d}{d\omega}\left(\angle G_{PM}(j\omega)\right) = 0 \tag{28}$$

and thus, accounts for:

$$\omega_{\Phi_{max}} = \sqrt{\omega_I \cdot \omega_{II}} \tag{29}$$

The phase response must be either lifted or lowered at the point of the gain crossover frequency, so that

$$\omega_{\Phi_{max}} = \omega_d = \omega_P \tag{30}$$

applies. The magnitude of the modulation of the phase response controller is determined by means of equation (27)

$$\begin{aligned}\Delta\Phi_{PM}(\omega_d) &\stackrel{!}{=} \angle G_{PM}(j\omega_{\Phi_{max}}) \\ &= \arcsin\left(\frac{m_{PM}-1}{m_{PM}+1}\right)\end{aligned} \tag{31}$$

and by the correction factor m_{PM} that is defined as the ratio of the cut-off frequencies

$$m_{PM} = \frac{\omega_{II}}{\omega_I} \tag{32}$$

Thus, the correction factor is expressed by

$$m_{PM} = \frac{1+\sin\left(\Delta\Phi_{PM}(\omega_d)\right)}{1-\sin\left(\Delta\Phi_{PM}(\omega_d)\right)} \tag{33}$$

and it is derived using equation (23). Eventually, the cut-off frequencies of the phase response controller are calculated by

$$\omega_I = \frac{1}{\sqrt{m_{PM}}}\cdot\omega_P \tag{34}$$

and

$$\omega_{II} = \sqrt{m_{PM}}\cdot\omega_P \tag{35}$$

In place of the gain crossover frequency, the gain response of the control loop is either lifted or lowered by the amount of $\sqrt{m_{PM}}$. This deviation must be compensated by the controller, so that in completion, the transfer function of the phase response controller is defined by

$$G_{PM}(s) = k_{0dB}\cdot\frac{1}{\sqrt{m_{PM}}}\cdot\frac{1+\omega_I^{-1}s}{1+\omega_{II}^{-1}s} \tag{36}$$

The gain response controller $G_{GM}(s)$

Besides the modulation of the phase response, a second controller shapes the gain response of the respective pendulum transfer function, on the basis of the open loop

$$G_0(s) = G_{PM}(s)\cdot G_S(s) \tag{37}$$

in order to adjust the gain margin A_{GM} according to the previously defined parameter range in equation (16). Due to the specific dynamic of $G_0(s)$ – it depends on the flight case and the G_{PM}-controller –, the need for either lifting or lowering the gain response in place of the phase crossover frequency $\omega_{-180°}$ is stated. For the modulation, another controller of the same kind like the phase response controller in equation (24) is defined and connected to $G_{PM}(s)$ in series:

$$G_{GM}(s) = \frac{1+\omega_{III}^{-1}s}{1+\omega_{IV}^{-1}s} \tag{38}$$

The gain response of the controller frequency response realizes a stationary correction of the amplitude for high frequencies $\omega\rightarrow\infty$, which is expressed by the correction factor

$$m_{GM} = \frac{\omega_{III}}{\omega_{IV}} \tag{39}$$

The quantitative demand on lifting or lowering in place of the phase crossover is derived by the difference of the desired and the current gain margin

$$\Delta A_{GM} = -\left(A_{GM,cmd} - A_{GM}(\omega_{-180°})\right)_{dB} \tag{40}$$

and results in

$$m_{GM} = 10^{\frac{\Delta A_{GM}}{20}} \tag{41}$$

The cut-off frequencies ω_{III} and ω_{IV} must be lower than those of the phase response controller in order to avoid a re-modification of the phase response in the frequency range that is relevant for flight mechanics. Thus, the upper cut-off frequency is defined to be much lower than the gain crossover frequency:

$$\omega_{III} \ll \omega_d \tag{42}$$

With the presetting of the upper cut-off frequency, the frequency ω_{IV} is determined according to (39), (40), and (41), considering the required gain margin to be within the range of (17).

Depending on the quantitative demand on ΔA_{GM}, the controller $G_{GM}(s)$ either lifts or lowers the phase in the low-frequency region ($\omega\in[\omega_{III},\omega_{IV}]$) and thus, either lifts or lowers the gain in the frequency range of the flight dynamics ($\omega\in[0.1,10]$).

The application of $G_{GM}(s)$ leads to an additional displacement of the gain response, causing the gain crossover frequency to be disarranged. A correction of this offset would lead to a change in phase margin, again. Thus, the displacement of ω_d remains at this point, but will be evaluated unfavorably in the performance index of section 5.

Eventually, the overall controller for shaping the frequency responses of both tansfer functions – $G_{\delta a\,\dot{\varphi}_P}(s)$ and $G_{\delta b\,\dot{\vartheta}_P}(s)$ – according to the dynamic requirements is defined as

$$\begin{aligned}G_R(s) &= G_{PM}(s)\cdot G_{GM}(s) \\ &= \frac{k_{0dB}}{\sqrt{m_{PM}}}\cdot\frac{1+\omega_I^{-1}s}{1+\omega_{II}^{-1}s}\cdot\frac{1+\omega_{III}^{-1}s}{1+\omega_{IV}^{-1}s}\end{aligned} \tag{43}$$

5 Optimization Algorithm

The parameters of each controller $(G_R)_{\delta a \dot{\varphi}_P}$ and $(G_R)_{\delta b \dot{\vartheta}_P}$ are derived by means of an optimization algorithm. The objective is the achievement of the requirements defined in equations (16), (17), and (18) by the open loop $G_0(s)$. The performance is then rated by the attained percental correlation of the target values. In addition, a high static amplification is regarded favorably.

The variation parameters of the optimization algorithm are given with the desired phase margin $\Phi_{PM,cmd}$ and the upper cut-off frequency ω_{III} of the gain response controller $G_{GM}(s)$. Due to a varying presetting of the phase margin, it then becomes feasible to differ in the theoretical optimum of 90° for the benefit of a better gain margin and gain crossover frequency, respectively. The presetting of ω_{III} allows for a distinct assignment of the scope of effectiveness of the gain response controller, in order to not interfere with the phase response, but shape the gain response for the better.

Figure 9 shows the process of the determination of the controller parameters. At first, a flight case – defined by the flight speed, the sling length, and the load weight – is selected, trimmed, and linearized. Thereupon, the simplified pendulum frequency ω_P is derived, and the step sizes of the variation parameters $\Phi_{PM,cmd}$ and ω_{III} are configured. Subsequent to the lifting of the gain response by the factor k_{0dB} up to the correlation of ω_d with ω_P, a search algorithm detects the phase margin $\Phi_{PM}(\omega_d)$. Hence, the quantitative demand $\Delta\Phi_{PM}$ on modulating the phase response is calculated. According to the equations (32) through (36), the controller parameters are derived for the specific flight case and the current presetting parameters.

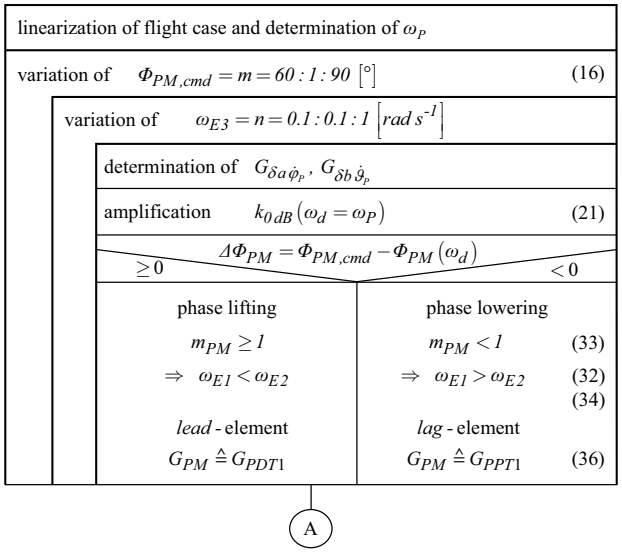

Figure 9: Determination of the phase response controller $G_{PM}(s)$

The quantitative demand on modulating the gain response ΔA_{GM} is determined by means of equation (40). The desired gain margin $A_{GM,cmd}$ is set to $-12\,dB$, as the average of the requirement formulated in (17).

The current amplitude in place of the phase crossover frequency $\omega_{-180°}$ is determined by means of another search algorithm that scans the gain response of the open loop according to (37). A secondary condition defines the gain of the pendulum poles to be $0.5\,dB$ at the minimum – compare eigenmodes *III* and *IV* in figure 8. Hereby, it is accomplished that the static amplification cannot become arbitrary low for the benefit of an optimal gain margin, by what quickness and effectiveness of the closed loop would decrease significantly. Hence, by deriving ΔA_{GM} and by considering the presetting ω_{III} of the optimization algorithm, the controller parameters are defined according to equations (39) through (41). The development process of the gain response controller is once more described in figure 10.

In case of a minor gain margin ($\Delta A_{GM} \geq 0$) together with a sufficiently high pendulum amplitude ($\Delta A_{corr} \geq 0$), the gain response is lowered until either the $0.5\,dB$-border or the required $A_{GM,cmd}$ is achieved. If the gain margin is too high ($\Delta A_{GM} < 0$), the gain response will be lifted up to $-12\,dB$.

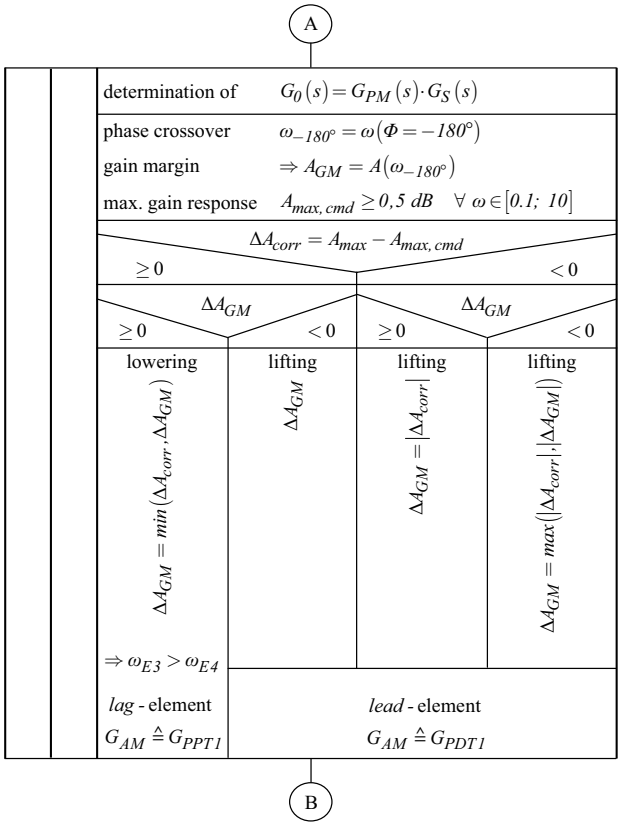

Figure 10: Determination of the gain response controller $G_{GM}(s)$

In a third case, the amplitude of the pendulum eigenmode may be too low. Hence, the gain response is lifted, but – in case of a minor gain margin ($\Delta A_{GM} \geq 0$) – only up to the required $0.5\,dB$, in order to not move away from the optimium of $-12\,dB$ more than necessary. If with ($\Delta A_{GM} < 0$) the gain margin is too high instead, the gain response is lifted up to $-12\,dB$ or at least up to $0.5\,dB$ of the pendulum eigenmode.

The calculation of the performance index J is shown in figure 11. At first, the performance parameters ω_d, A_{GM}, and Φ_{PM} are derived by analyzing the open loop according to

$$(44) \quad G_0(s) = G_{PM}(s) \cdot G_{GM}(s) \cdot G_S(s)$$

For the subsequent use in the perfomance index, the percental values of the parameters are considered in order to have a common basis of evaluation. The conversion for all three parameters is accomplished by

$$(45) \quad \Lambda_{\%} = \begin{cases} \frac{\Lambda^+}{\Lambda^*} \cdot 100\% & , (\Lambda^+ \leq \Lambda^*) \\ \left(-\frac{\Lambda^+ - \Lambda^*}{\Lambda^*} + 1\right) \cdot 100\% & , (\Lambda^+ > \Lambda^* \wedge \\ & \quad \Lambda^+ \leq 2 \cdot \Lambda^*) \end{cases}$$

applying for

- $\Lambda_{\%} = (\Phi_{PM,perc}, A_{GM,perc}, \omega_{d,perc})$
- $\Lambda^+ = (\Phi_{PM}(\omega_d), A_{GM}(\omega_d), \omega_d)$
- $\Lambda^* = (\Phi_{PM,cmd}, A_{GM,cmd}, \omega_P)$

The procentual correlations of the performance parameters – they describe the dynamic of the respective open loop – are weighted and merged into the perfomance index J in equation (46)

$$(46) \quad J_{n,m} = K_V \left(\omega_{d,perc} + \left(\Phi^3_{PM,perc} + A^3_{GM,perc}\right) \cdot 10^{-4}\right)$$

considering

$$(47) \quad \begin{aligned} n &= \Phi_{PM,cmd} \in [60, 90] \\ m &= \omega_{III} \in]0, 1] \end{aligned}$$

The weighting of the static amplification according to

$$(48) \quad K_V = \left(\frac{k_{0\,dB}}{\sqrt{m_{PM}}}\right)^{1/8}$$

causes small values of K_V to be evaluated unfavorably, which leads to a decrease in J, since a low magnitude

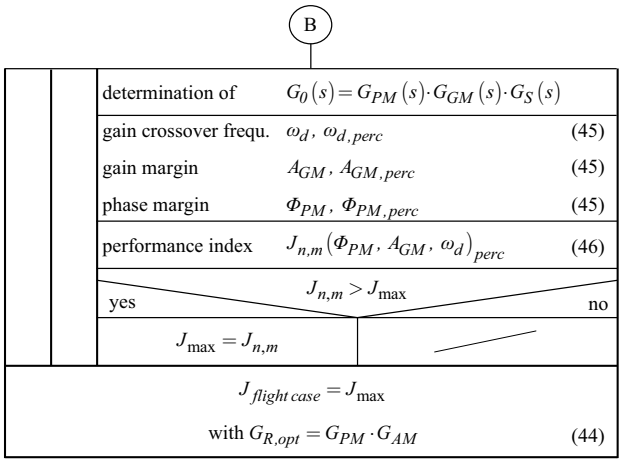

Figure 11: Calculation of the performance index

of the static amplification means a decline in the controller's effectiveness. However, very high amplifications are also weighted unfavorably. Relevant analyses showed that an exponent of 1/8 guarantees a well-balanced weighting of either very low or very high static amplifications, so that mean amplifications are considered favorably.

In addition, the weighting of the procentual correlations of the performance parameters is different. Deviations of the closed loop from $\Phi_{PM,cmd}$ and $A_{GM,cmd}$ are penalized stronger than deviations from the gain crossover frequency. Hereby, it is expressed that the requirements of stability, and a sufficient damping, and robustness are more important than the quickness of the control loop.

Finally, the optimal pendulum damping controller of the considered flight case is derived by the determination of the maximum performance value:

$$(49) \quad J_{max} = max\,(J_{n,m})$$

over the variation of $\Phi_{PM,cmd}$ and ω_{III}.

6 Closed-Loop Analysis

Starting from the flight case at $V = 60\,kts$, $l_S = 7\,m$, and $m_L = 500\,kg$, some optimal pendulum damping controllers are derived by means of the optimization algorithm. The sensitivity of the controller parameters is analyzed regarding a variation of the sling length and the load weight, in order to detect relations between the controller design parameters and the dynamic results, expressed by the performance index.

Figure 12 shows the parameters of the longitudinal pendulum controller for the flight case and a variation of the load weight from $300\,kg$ up to $4000\,kg$. Besides the attainable performance index J_{max} and the static amplification K_V, the intervals between the cut-off frequencies of the phase response controller and the gain

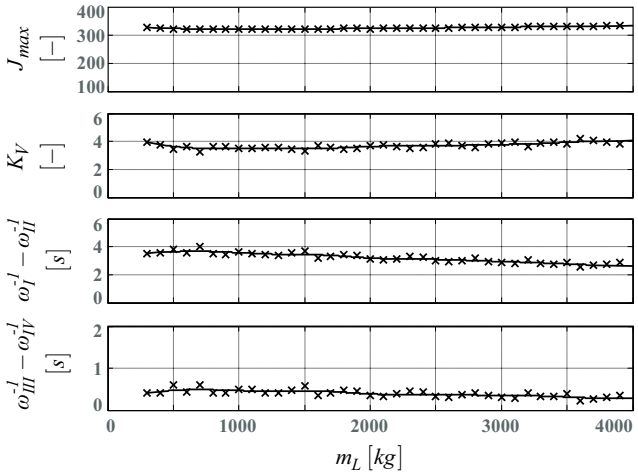

Figure 12: $(G_R)_{\delta b\,\dot{\vartheta}_P}$ controller parameter analysis at $60\,kts$ and $l_S = 7\,m$

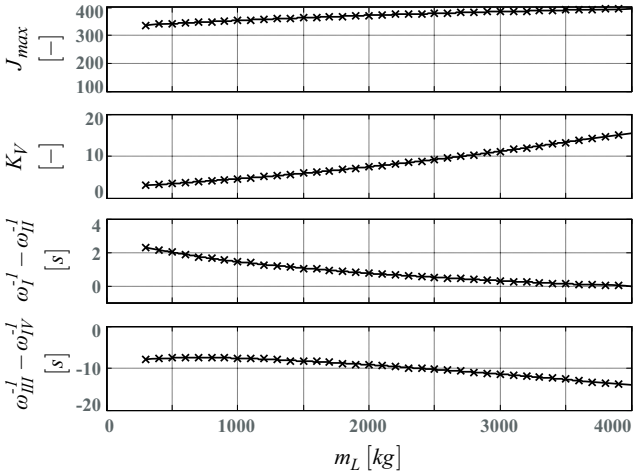

Figure 13: $(G_R)_{\delta a\,\dot{\varphi}_P}$ controller parameter analysis at $60\,kts$ and $l_S = 7\,m$

response controller are illustrated. In case of a positive interval, the respective controller works either phase lifting or gain lifting; otherwise, phase and gain response are lowered. The intensity of correction is defined by the magnitude of the interval: The larger the distances of the cut-off frequencies are, the greater the correction is. The figure at hand reveals that for the derivation of high performance indices, the controller parameters do not vary considerably in case of a change in load weight. The static amplification as well as the intensity of both controllers remain fairly constant. The positive values of the distances of the cut-off frequencies characterize a phase lift in place of the gain crossover frequency and a gain lift in place of the phase crossover frequency, respectively. That means – independent on the load weight – that for the longitudinal pendulum damping, the phase margin is enlarged and the gain margin is decreased in order to meet the requirements on the dynamics of the closed loop. Further tests for $20\,kts$ and $100\,kts$ showed that this conclusion applies also for a change in flight speed.

As before, the parameters of the lateral pendulum controller are analyzed in figure 13 in case of a variation of the load weight at $60\,kts$ flight speed and a sling length of $7\,m$. It can be seen that with an increase in load weight, greater static amplifications K_V are achievable, and the maximum performance index rises. At the same time, the demand on enlarging the phase margin decreases, which is indicated by the falling interval of $(\omega_I^{-1} - \omega_{II}^{-1})$ of the phase response controller. However, the gain response must be lowered significantly, in case of an increase in load weight.

The analysis in section 3 showed that the flight dynamic of the pendulum motions is changed in particular with a change in sling length. Consequently, the parameter variations of both, the longitudinal and the lateral pendulum damping controllers, are displayed in figures 14 and 15. In the former case, a great demand

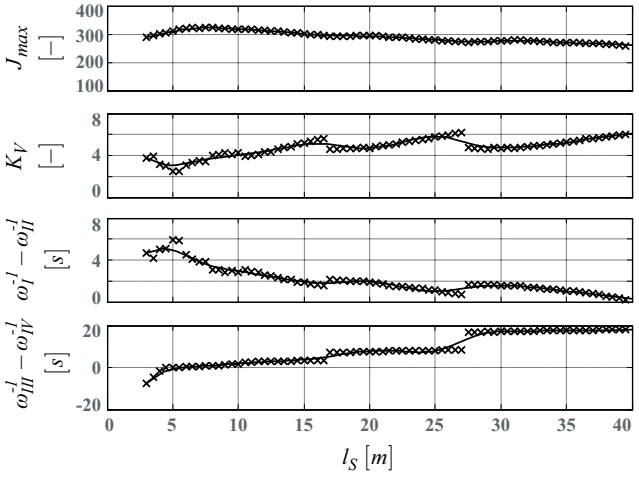

Figure 14: $(G_R)_{\delta b\,\dot{\vartheta}_P}$ controller parameter analysis at $60\,kts$ and $m_L = 500\,kg$

on lifting the phase response and decreasing the gain response is required in order to enlarge the gain margin for short slings. By enlongating the slings, the intensity of the controllers declines, because the phase margin of the open loop is enlarged and its gain response is lowered, respectively. From a sling length of approximately $8\,m$ up, the gain response is lifted by $G_{GM}(s) = f(\omega_{III}, \omega_{IV})$. The natural raise of the phase margin leads to a decrease in the intensity of the phase response controller $G_{PM}(s) = f(\omega_I, \omega_{II})$. Due to the increase in stability margins, the static amplification K_V is enlarged. In general, it can be seen that the performance of the controllers is degraded for very short ($\approx 3\,m$) and very long ($> 30\,m$) slings, respectively.

The discontinuous developing of the parameter curves results from the step sizes of the design parameters $\Phi_{PM,cmd}$ and ω_{III}. As advanced analyses show, the basic characteristics of the parameter variations in

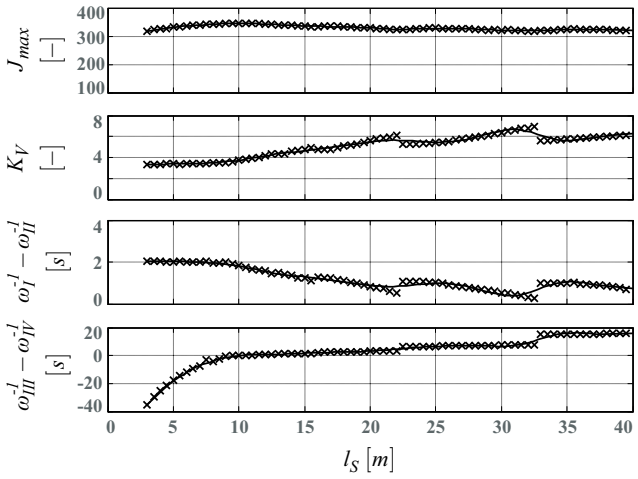

Figure 15: $(G_R)_{\delta a\,\dot{\varphi}_P}$ controller parameter analysis at $60\,kts$ and $m_L = 500\,kg$

case of a change in sling length also apply for $20\,kts$ and $100\,kts$.

Similar to the change in parameters for the longitudinal controller, a variation in sling length affects the lateral pendulum damping controller (fig. 15). For very short slings, the controller loweres the gain response; in case of very long slings, it is lifted. The controller performance remains sufficiently high over the parameter variation. However, as further analyses revealed, the performance is decreasing with increasing flight speed.

The analysis of the variation of the eigenmodes pointed out that the helicopter dutch roll mode in *II* was destabilized by the longitudinal pendulum damping controller to such an extent that it became unstable at low amplifications, already. Hence, the pitch rate feedback of the AFCS was increased. The influence of the pendulum controller on the root locus of the eigenmodes of the closed loop $G_{\delta b\,\dot{\varphi}_P}$ is shown in figure 16a. It can be seen that the damping of the longitudinal pendulum motion in *IV* is increased at the optimal amplification k_{opt}, without destabilizing the helicopter in *II* significantly. The roll mode in *VI* merges with the controller to an oscillation. Furthermore, the ⧫-symbol marks the amplification that is feasible until the damping of the helicopter mode in *II* decreases below $\zeta < 0.3$.

The root locus of the laterally controlled pendulum motion is displayed in figure 16b. Like before, the helicopter dynamics in *I* and *II* are slightly rearranged. However, the lateral feedback of the AFCS was not adjusted.

In section 2, cylinder aerodynamics have been added to the rigid-body dynamics. The stability graph of the cylinder eigenmodes is shown in figure 5. In a next step, the pendulum damping performance of the controllers in the time domain is analyzed. For this, a trimmed level flight at $V = 60\,kts$, $l_S = 10\,m$, and $m_L = 500\,kg$ is considered. The helicopter is disturbed by a 15%-pulse input in lateral control δa (fig. 17a).

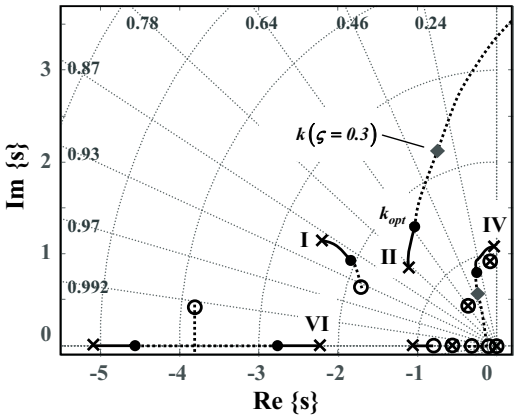

(a) $G_{\delta b\dot{\varphi}_P}$

(b) $G_{\delta a\dot{\vartheta}_P}$

Figure 16: Root locus graphs for the flight case $V = 60\,kts$, $l_S = 7\,m$, $m_L = 3000\,kg$

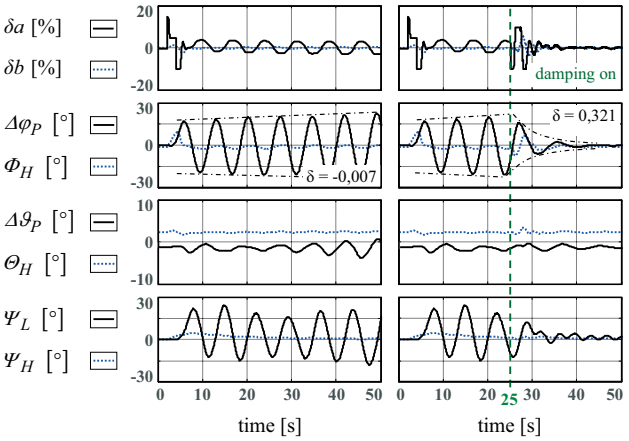

(a) damping inactive (b) damping active

Figure 17: Damping of the unstable pendulum oscillation of the cylinder at $V = 60\,kts$, $m_L = 500\,kg$, and $l_S = 10\,m$

Hence, the cylinder develops an unstable coupled roll-yaw-oscillation in (φ_P, Ψ_L) as expected. In the upper pane of figure 17a, it can be seen that the lateral control is periodically deflected: Due to the coupling between the sling load (φ_P, ϑ_P) and the helicopter (Φ_H, Θ_H), the load oscillation induces rolling moments to the helicopter. The AFCS tries to compensate the helicopter dynamics, without success. In figure 17b, the same flight test is displayed until at $t = 25\,s$, the 2-axes-pendulum-damping controller is activated. Within the range of the controller limiter, the unstable roll-yaw-oscillation is damped rapidly and sustainably. Due to the inflow at the vertical fin, a slight dynamic in yaw remains over time.

7 Conclusion and Outlook

Sling loads influence the helicopter dynamics. The handling qualities are degraded and the pilot workload is increased significantly due to the additional task to control the load. Hence, not only the helicopter's operational range and its flight envelope are reduced, but also flight safety is decreased. The need for pilot support is therefore evident: The paper at hand focusses on the development of supplementary AFCS-modes, which generate control inputs that eventually damp lateral and longitudinal load oscillations.

On the basis of a comprehensive system simulation featuring trim-calculation, linearization and virtual flight testing, load pendulum damping controllers are developed by means of an automatic optimization algorithm. Analyses show that the pendulum dynamic can be damped sufficiently over a broad range of parameter variations in sling length, load weight, and flight speed. The controllers are effective within the operating range of the AFCS-actuators regarding the limited rate and saturation.

In a next step, the controller algorithm and the digital image processing system will be implemented into the DLR system simulator and the Flying Helicopter Simulator (FHS) in order to analyze the controller effectiveness for different helicopter types, and to evaluate pilot acceptance.

Appendix

Rigid-body dynamics

In a first step, the helicopter and load are described separately as two independent six degree-of-freedom rigid bodies. The general equations of the nonlinear translational and rotatory motions are given by (50) and (51) (q.v. app.). The index $\Lambda = (H, L)$ enunciates the compatibility of the equations for the helicopter and the load, respectively. For the validity of (50) and (51) following conditions apply:

- the earth is considered as initial frame
- the helicopter and the load are considered as rigid bodies
- the helicopter and the load are symmetric relating to the xz-plane, leading to $I_{xy} = I_{yz} = 0$
- external forces are concentrated in resultant forces acting in the respective center of gravity

The rod is considered as additional body with two degrees of freedom; its dynamics is determined by angular-moment-theory in equation (53).

Therefore, the dynamics of the overall system is described by the states

$$\begin{aligned} \boldsymbol{x}_H &= (u, v, w, p, q, r, \Phi, \Theta)_H \\ \boldsymbol{x}_L &= (u, v, w, p, q, r, \Phi, \Theta)_L \\ \boldsymbol{x}_R &= \left(\dot{\varphi}, \dot{\vartheta}\right)_R \end{aligned}$$

The general nonlinear equation of the translational motion is given by:

$$\left(\frac{d\boldsymbol{V}}{dt}\right)_{\Lambda,b} = \frac{1}{m_\Lambda} \cdot \sum \boldsymbol{F}_{\Lambda,b} - \boldsymbol{\omega}_{\Lambda,b} \times \boldsymbol{V}_{\Lambda,b} \tag{50}$$

and of the rotation by:

$$\left(\frac{d\boldsymbol{\omega}}{dt}\right)_{\Lambda,b} = \boldsymbol{I}_{\Lambda,b}^{-1} \cdot \left[\sum \boldsymbol{M}_{\Lambda,b}^{CG} - \boldsymbol{\omega}_{\Lambda,b} \times \left(\boldsymbol{I}_{\Lambda,b}^{-1} \cdot \boldsymbol{\omega}_{\Lambda,b}\right)\right] \tag{51}$$

applying for the helicopter and the load $(\Lambda = (H, L))$.

The rod is considered as additional body with two degrees of freedom:

$$\left(\frac{d\boldsymbol{\omega}}{dt}\right)_{R,b} = \left(\ddot{\varphi}, \ddot{\vartheta}\right)_R^T \tag{52}$$

The analytical modeling is based on angular-moment-theory for systems, whose reference point is neither its center of gravity nor its fixed-point:

$$\left(\frac{d\boldsymbol{\omega}}{dt}\right)_{R,b} = \left(\boldsymbol{I}_{R,b}^{LH}\right)^{-1} \cdot \left[\sum \boldsymbol{M}_{R,b}^{LH} - m_R \cdot \left(\boldsymbol{r}_{LH \to R} \times \boldsymbol{a}_{LH,g}^{abs}\right)\right] \tag{53}$$

The sum of the resulting moments with respect to the

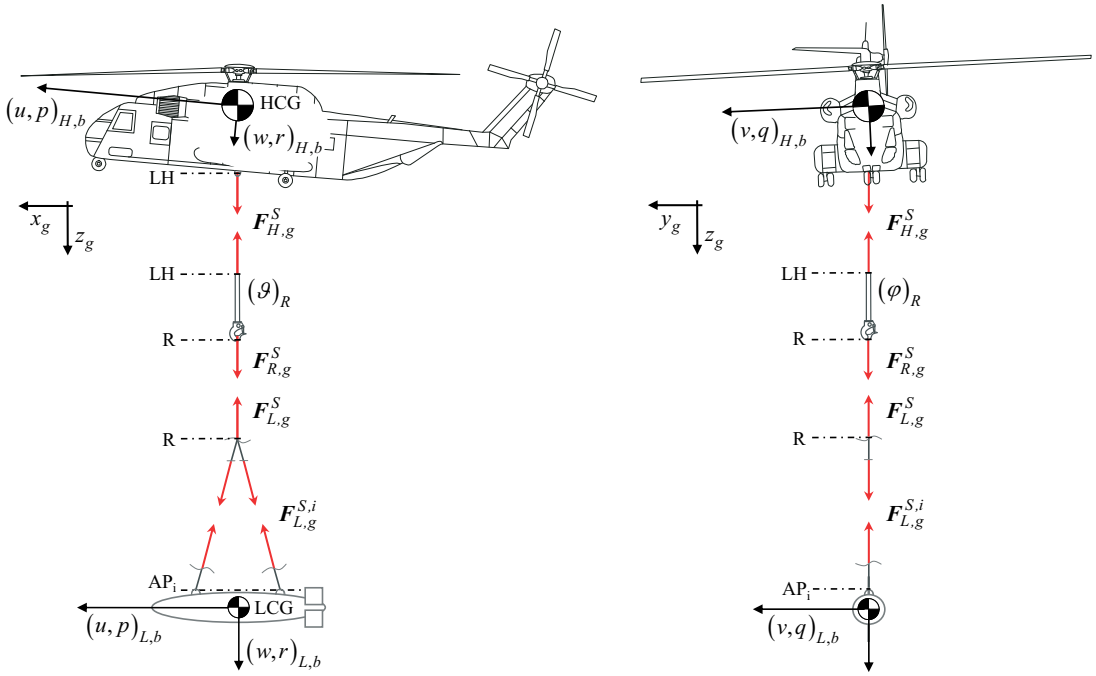

Figure 18: Overall system *helicopter, rod and sling load*

load hook is derived by

$$\sum \boldsymbol{M}^{LH}_{R,b} = -\frac{l_R\, m_R\, g}{2} \cdot \begin{bmatrix} \sin\varphi\, \cos\vartheta \\ \cos\varphi\, \sin\vartheta \\ \cos\varphi\, \cos\vartheta \end{bmatrix}_R + \begin{bmatrix} 0 \\ 0 \\ l_R \end{bmatrix} \times \boldsymbol{F}^{sling}_R \tag{54}$$

The absolute acceleration of the helicopter load hook in the geodetic system is obtained by

$$\boldsymbol{a}^{abs}_{LH,g} = \boldsymbol{TM}^{H}_{gb} \cdot \boldsymbol{a}^{abs}_{LH,b} \tag{55}$$

and the absolute acceleration of the load hook in helicopter body-axes:

$$\begin{aligned} \boldsymbol{a}^{abs}_{LH,b} = \boldsymbol{a}^{abs}_{H,b} &+ \underbrace{\dot{\boldsymbol{\omega}}_{H,b} \times \boldsymbol{r}_{HCG\to LH}}_{\text{tangential acc.}} \\ &+ \underbrace{\boldsymbol{\omega}_{H,b} \times (\boldsymbol{\omega}_{H,b} \times \boldsymbol{r}_{HCG\to LH})}_{\text{centripetal acc.}} \\ &+ \underbrace{2 \cdot \boldsymbol{\omega}_{H,b} \times \boldsymbol{v}^{rel}_{LH,b}}_{\text{coriolis acc.}} + \boldsymbol{a}^{rel}_{LH,b} \end{aligned} \tag{56}$$

The distance between the helicopter center of gravity and the load hook remains constant. Hence, the relative acceleration $\boldsymbol{a}^{rel}_{LH,b}$ as well as the coriolis acceleration, both become zero.

The external forces and moments in the equations (50), (51), and (53) result from aerodynamics and the sling forces.

Aerodynamics

The tangential forces of the cylinder result from skin friction and impact pressure, and are summed up according to:

$$X_{L,b} = \frac{\rho}{2} V_x^2 \left(S_{F,C}\, C_f + S_{S,C}\, C_{press,0}\right) \tag{57}$$

The normal forces are derived by

$$Z_{L,b}(\alpha) = \frac{\rho}{2} V_{xz}^2\, S_C\, C_{D0} \sin^2(\alpha) \tag{58}$$

for the xz-plane with the angle of attack α and by

$$Z_{L,b}(\beta) = \frac{\rho}{2} V_{xy}^2\, S_C\, C_{D0} \sin^2(\beta) \tag{59}$$

for the xy-plane with the angle of sideslip β. The resulting aerodynamic forces acting in the cylinder body axes are given by:

$$\boldsymbol{F}^A_{L,b} = \frac{\rho}{2} \cdot \begin{pmatrix} \left(S_{S,C}\, C_{press,0} + S_{F,C}\, C_f\right) V_x^2 \\ V_{xy}^2\, S_C\, C_{D0} \sin^2(\beta) \\ V_{xz}^2\, S_C\, C_{D0} \sin^2(\alpha) \end{pmatrix} \tag{60}$$

where the drag coefficient is derived by [11, p.3-11]:

$$C_{D0} = \begin{cases} 2\, C_{f,lam.} \left(1 + \frac{c_E}{b_E}\right) + 1{,}1 \left(\frac{b_E}{c_E}\right) \\ \quad \text{if } (Re < Re_{crit}) \\ 2\, C_{f,turb.} \left(4 + 2\left(\frac{c_E}{b_E}\right) + 120 \left(\frac{b_E}{c_E}\right)^2\right) \\ \quad \text{if } (Re \geq Re_{crit}) \end{cases} \tag{61}$$

The surface of the cylinder is given with $S_C = d_C\, l_C$, and the surface passed by flow with $S_{F,C} = 0.5\,\pi\, d_C\, l_C$, and the cross section surface with $S_{S,C} = 0.25\,\pi\, d_C^2$.

The frictional resistance changes with the transition from laminar ($C_f = 0.0075$) to turbulent flow ($C_f = 0.005$). The actual flow condition is distinguished by the critical Reynolds number $Re_{crit} = 10^5$ [11, p.2-1].

The aerodynamic moments of the cylinder are given by

$$\boldsymbol{M}^A_{L,b} = \frac{\rho}{2} \cdot V_C \begin{pmatrix} 0 \\ V_{xz}^2\ (k_2 - k_1)\ \sin(2\alpha) \\ V_{xy}^2\ (k_2 - k_1)\ \sin(2\beta) \end{pmatrix} \tag{62}$$

The parameters k_1 and k_2 are derived from

$$k_1 = a_C b_C c_C \int_0^\infty \frac{dp}{(a_C^2+p)\sqrt{(a_C^2+p)(b_C^2+p)(c_C^2+p)}}$$
$$k_2 = a_C b_C c_C \int_0^\infty \frac{dp}{(b_C^2+p)\sqrt{(a_C^2+p)(b_C^2+p)(c_C^2+p)}} \tag{63}$$

with $a_C = 0.5\, l_C$, and $b_C = c_C = 0.5\, d_C$ as semiaxes of the spheroid [12, p.104].

The aerodynamic forces and moments of the vertical fin are added to those of the cylinder:

$$\boldsymbol{F}^A_{F,b} = -\frac{\rho}{2} V_{xy}^2 S_F \cdot \boldsymbol{TM}_{ba} \cdot \begin{pmatrix} C_{D\beta} \\ C_{L\beta} \\ 0 \end{pmatrix} \cdot \beta \tag{64}$$

The fin is modelled as a symmetric *NACA-0015* airfoil, whose aerodynamic characteristics – especially the drag and lift coefficients – were determined over the full range of 180°-angle of attack [13]. In the range of ($0° < \beta < 20°$) as well as ($160° < \beta < 180°$), aerodynamics are calculated for laminar circulation. In case of angles of attack in the range of ($45° < \beta < 135°$), the fin is attacked laterally with the consequence of turbulent circulation and stall effects: Only pressure forces occur. For the transition regions ($20° < \beta < 45°$) and ($135° < \beta < 160°$), linear characteristics apply. The aerodynamic moments of the vertical fin are added to those of the cylinder and are derived by

$$\boldsymbol{M}^A_{F,b} = \boldsymbol{F}^A_{F,b} \times \boldsymbol{r}_{F,b} \tag{65}$$

with $\boldsymbol{r}_F$ as the distance from the center of pressure of the fin to the center of gravity of the cylinder.

Constraining forces

The resultant vector of the sling forces in the respective body system ($\Lambda = H, R, L$) is given by the transformation of the vectors of the geodetic sling forces

$$\boldsymbol{F}^S_{\Lambda,b} = \boldsymbol{TM}^\Lambda_{bg} \cdot \sum_i \boldsymbol{F}^{S,i}_{\Lambda,g} \tag{66}$$

derived by the vectorial description of the sling force

$$\boldsymbol{F}^{S,i}_{\Lambda,g} = \left|\boldsymbol{F}^{S,i}\right| \cdot \begin{pmatrix} \sin\vartheta \cdot \cos\varphi \\ \cos\vartheta \cdot \sin\varphi \\ \cos\vartheta \cdot \cos\varphi \end{pmatrix}^{S,i}_g \tag{67}$$

which is determined for each sling due to its elongation and elongation rate:

$$\left|\boldsymbol{F}^{S,i}\right| = c_{S,i}\, \Delta l_{S,i} + d_{S,i}\, \dot{l}_{S,i} \tag{68}$$

The attitude of each sling is given by (q.v. fig.18):

$$\varphi^{S,i}_g = -\arctan\left(\frac{y_{AP} - y_R}{z_{AP} - z_R}\right)^{S,i}_g \tag{69}$$

$$\vartheta^{S,i}_g = -\arctan\left(\frac{x_{AP} - x_R}{z_{AP} - z_R}\right)^{S,i}_g \tag{70}$$

The moment vectors due to the sling forces in the helicopter and load body system are given by

$$\boldsymbol{M}^S_{H,b} = \left[\begin{bmatrix} x \\ y \\ z \end{bmatrix}^{LH}_{H,b} - \begin{bmatrix} x \\ y \\ z \end{bmatrix}^{HCG}_{H,b} \right] \times \boldsymbol{F}^S_{H,b} \tag{71}$$

and

$$\boldsymbol{M}^{S,i}_{L,b} = \left[\begin{bmatrix} x \\ y \\ z \end{bmatrix}^{AP,i}_{L,b} - \begin{bmatrix} x \\ y \\ z \end{bmatrix}^{LCG}_{L,b} \right] \times \boldsymbol{F}^{S,i}_{L,b} \tag{72}$$

References

[1] Shaughnessy, J.D. ; Pardue, M.D.: Helicopter Sling Load Accident/Incident Survey: 1968-1974 / NASA. 1977. – Technical Report

[2] Harris, F.D. ; Kasper, E.F. ; Iseler, L.E.: U.S. Civil Rotorcraft Accidents, 1963 through 1997 / NASA. 2000. – Technical Report

[3] NN: US Joint Helicopter Safety Team: Year 2000 Report / International Helicopter Safety Team (IHST). 2007. – Technical Report

[4] Brenner, H.: Flight Testing of Pioneer Bridges as Helicopter Slung Loads Using a CH-53G. In: *Proceedings of the 33rd European Rotorcraft Annual Forum*, 2007

[5] Hamers, M. ; Hinüber, E. von ; Richter, A.: CH53G Experiences with a Flight Director for Slung Load Handling. In: *Proceedings of the American Helicopter Society 64th Annual Forum*, 2008

[6] Cicolani, L.S. ; Raz, R. ; Ronen, R.: Flight Test, Simulation and Passive Stabilization of a Cargo Container Slung Load in Forward Flight. In: *Proceedings of the American Helicopter Society 63rd Annual Forum*, 2007

[7] Heffley, R.K. ; Jewell, W.F.: A Compilation and Analysis of Helicopter Handling Qualities Data - Volume One: Data Compilation / NASA Contractor Report 3144. 1979. – Technical Report

[8] Etkin, B.: Stability of a Towed Body. In: *Journal of Aircraft* 35 (1998)

[9] *iMAR-GmbH, Gesellschaft für inertiale Mess-, Automatisierungs- und Regelsysteme.* `http://www.imar-navigation.de`

[10] Cicolani, L.S. ; McCoy, A.H. ; Tischler, M.B. ; Tucker, G.E.: Flight Time Identification of a UH-60A Helicopter and Slung Load, TM-1998-112231 / NASA Ames Research Center. 1998. – Technical Report

[11] Hoerner, S.F.: *Fluid-Dynamic Drag, Practical Information on Aerodynamic Drag and Hydrodynamic Resistance.* 1965

[12] Ames, J.S.: A Resume of the Advances in Theoretical Aeronautics made by Max M. Munk, Report No. 213 / NACA. 1926. – Technical Report

[13] Sheldal, R. ; Klima, P.: Aerodynamic Characteristics of Seven Symmetrical Airfoil Sections Through 180-Degree Angle of Attack for Use in Aerodynamic Analysis of Vertical Axis Wind Turbines / Sandia National Laboratories, Albuquerque. 1981. – Technical Report